AIP | Physics of Plasmas

Inertial confinement fusion implosions with imposed magnetic field compression using the OMEGA Laser

M. Hohenberger, P.-Y. Chang, G. Fiksel, J. P. Knauer, R. Betti et al.

Citation: Phys. Plasmas **19**, 056306 (2012); doi: 10.1063/1.3696032
View online: http://dx.doi.org/10.1063/1.3696032
View Table of Contents: http://pop.aip.org/resource/1/PHPAEN/v19/i5
Published by the American Institute of Physics.

Inertial confinement fusion implosions with imposed magnetic field compression using the OMEGA Laser[a)]

M. Hohenberger,[1,2,3,b)] P.-Y. Chang,[1,2,4] G. Fiksel,[1,2] J. P. Knauer,[2] R. Betti,[1,2,3,4] F. J. Marshall,[2] D. D. Meyerhofer,[1,2,3,4] F. H. Séguin,[1,5] and R. D. Petrasso[1,5]
[1]*Fusion Science Center for Extreme States of Matter and Fast Ignition Physics, University of Rochester, 250 East River Road Rochester, New York 14623, USA*
[2]*Laboratory for Laser Energetics, University of Rochester, 250 East River Road Rochester, Rochester, New York 14623, USA*
[3]*Department of Mechanical Engineering, University of Rochester, 250 East River Road Rochester, Rochester, New York 14627, USA*
[4]*Department of Physics and Astronomy, University of Rochester, 250 East River Road Rochester, Rochester, New York 14627, USA*
[5]*Plasma Science and Fusion Center, MIT, Cambridge, Massachusetts 02139, USA*

(Received 7 December 2011; accepted 29 February 2012; published online 28 March 2012)

Experiments applying laser-driven magnetic-flux compression to inertial confinement fusion (ICF) targets to enhance the implosion performance are described. Spherical plastic (CH) targets filled with 10 atm of deuterium gas were imploded by the OMEGA Laser, compare Phys. Plasmas **18**, 056703 or Phys. Plasmas **18**, 056309. Before being imploded, the targets were immersed in an 80-kG magnetic seed field. Upon laser irradiation, the high implosion velocities and ionization of the target fill trapped the magnetic field inside the capsule, and it was amplified to tens of megagauss through flux compression. At such strong magnetic fields, the hot spot inside the spherical target was strongly magnetized, reducing the heat losses through electron confinement. The experimentally observed ion temperature was enhanced by 15%, and the neutron yield was increased by 30%, compared to nonmagnetized implosions [P. Y. Chang *et al.*, Phys. Rev. Lett. **107**, 035006 (2011)]. This represents the first experimental verification of performance enhancement resulting from embedding a strong magnetic field into an ICF capsule. Experimental data for the fuel-assembly performance and magnetic field are compared to numerical results from combining the 1-D hydrodynamics code *LILAC* with a 2-D magnetohydrodynamics postprocessor.
 [http://dx.doi.org/10.1063/1.3696032]

I. INTRODUCTION

In inertial confinement fusion (ICF),[1–3] a capsule consisting of cryogenic deuterium and tritium and filled with DT gas is rapidly compressed to high temperatures and areal densities sufficient for nuclear fusion reactions. Provided the α particles generated by the D-T reactions are confined and deposit their energy in the compressed core, the capsule ignites and the energy released via the fusion burn can exceed the energy driving the implosion, i.e., the fusion gain exceeds unity. Compression of the target in laser-driven ICF is pursued using two distinct methods: In the direct-drive scheme,[4,5] multiple laser beams irradiate the capsule uniformly, driving an ablative compression of the shell. In indirect drive,[6] the laser irradiates the inner walls of a cavity of high atomic number (Hohlraum), generating a thermal x-ray bath of 200–300 eV that drives the ablative capsule implosion. In both cases, at the end of the compression phase, the fuel assembly consists of a hot ($\sim$3–8 keV), moderate density ($\sim$30–100 g/cm^3) central hot spot, surrounded by a colder ($\sim$200–400 eV) but dense ($\sim$300–1000 g/cm^3) fuel layer.[7]

The requirements for hot-spot ignition, particularly the ion temperature, impose a lower limit on the shell implosion velocity V_i. It must be large enough so that the shell-imparted PdV work overcomes the core's thermal losses. For direct drive, it has been shown[8] that the hot-spot temperature scales with the implosion velocity V_i, as $T_h \propto V_i^{1.25}$. Increasing V_i requires enhanced drive and, therefore, more laser energy, thereby reducing the gain. The thermonuclear gain G of an ignited target can be related to the implosion velocity[9] via $G \propto 1/V_i^{1.25}$. Therefore, the minimum V_i imposed by thermal losses directly limits the gain achievable through ignition.

In the concept of magnetized ICF, additional thermal insulation of the hot spot is achieved by applying a strong magnetic field to an otherwise conventional ICF fuel assembly.[10,11] The results reported in Ref. 11 constitute the first experimental evidence of a fusion performance enhancement through magnetization of an ICF hot spot. These experiments were performed on the OMEGA Laser at the Laboratory for Laser Energetics (LLE).[12] In particular, a neutron yield enhancement of 30% and an ion temperature increase of 15% were observed. This paper discusses the experimental results of Ref. 11 in more detail. In addition, we report new results on measurements of the compressed magnetic field, compare the experimental results with numerical simulations, and elaborate on alternative magnetic configurations capable of providing a better thermal insulation.

Following the formalism developed by Braginskii,[13] the electron heat transport perpendicular to a straight magnetic-

[a)]Paper YI3 2, Bull. Am. Phys. Soc. **56**, 361 (2011).
[b)]Invited speaker.

field line is governed by the magnetization parameter $\omega_e\tau_e$, where ω_e is the electron gyrofrequency and τ_e is the electron collision time. Electron confinement and suppression of heat conduction are achieved for $\omega_e\tau_e > 1$. A magnetic confinement condition can also be formulated for the α particles generated during the burn stage of an ignited target. If the gyroradius r_α is of the order of the hot-spot radius R_h or smaller, i.e., $r_\alpha/R_h \leq 1$, the α particles are confined and predominantly deposit their energy in the burn region, limiting energy losses and maintaining the fusion burn for a longer time. Applying magnetic fields of sufficient magnitude to suppress energy losses can enhance fuel-assembly performance. This can be quantified via simple scaling arguments.[8] At ignition-relevant temperatures of $3< T_h <8$ keV, the fusion cross section scales as $\langle\sigma v\rangle \propto T_h^3$. The thermonuclear yield $Y \propto n^2\langle\sigma v\rangle$, with n denoting the particle density, scales with the hot-spot pressure and temperature as $Y \propto p^2 T_h$, such that an increase in the hot-spot temperature results in an enhanced yield. By enhancing the fuel-assembly performance and assuming the same laser drive conditions, more fuel material can be compressed at a lower implosion velocity while still reaching ignition conditions, leading to higher thermonuclear gain.[9]

To take advantage of the heat-loss suppression in a magnetized target, substantial magnetic fields are necessary. Using typical hot-spot conditions of $T_h = 5$ keV and $\rho_h = 30$ g/cm^3, the magnetic field required to achieve $\omega_e\tau_e > 1$ and magnetize the electrons is $B \gtrsim 10$ MG. Assuming a hot-spot radius of $R_h = 40$ μm, $B \gtrsim 70$ MG is needed to confine α particles.

Applying magnetic fields to an ICF scheme to improve the target performance is not a new idea. There is a long history of work considering adding magnetic fields to an ICF scheme (e.g., Refs. 14–16 and the references therein). Laser-driven magnetic-flux compression in cylindrical targets has been discussed theoretically by Choe.[17] Heat-flux suppression is the basis of magnetized target fusion, where a preformed magnetized plasma is compressed via a cylindrical liner implosion,[18] a concept that is being actively pursued both experimentally and analytically.[19,20]

This paper is organized as follows: Section II discusses the concept of magnetic-flux compression, which is used to reach the strong magnetic fields required to magnetize a hot spot. Section III contains details about the experimental platform MIFEDS that has been developed to undertake laser-driven magnetic-flux–compression experiments. Section IV reviews an initial series of experiments in which the concept of laser-driven magnetic-flux compression was demonstrated in cylindrical geometry. Section V presents experimental results from applying magnetic fields to spherically compressed targets. Section VI discusses numerical simulations of flux-compression experiments. Section VII discusses potential paths to a closed field-line topology inside an ICF target, and Sec. VIII presents our conclusions.

II. MAGNETIC-FLUX COMPRESSION

The main issue with magnetized ICF is how magnetic fields of 10–100 MG can be embedded into the hot spot of an ICF implosion.[10] Such strong fields are difficult to generate directly. Magnetic-flux compression represents a viable path to megagauss magnetic fields. A seed field of lower magnitude is embedded within a good conductor, followed by the compression of the enclosed area on a time scale that is fast enough to prevent resistive diffusion from causing the field to leak through (Fig. 1). Creating high magnetic fields by magnetic-flux compression has been pursued over several decades, for example, by imploding Z-pinches[21–24] or metal liners driven either electromagnetically[25,26] or with high explosives.[27] In ICF, the required magnetic fields for magnetization of a hot spot can be produced by 100- to 1000-fold compression of an ~100-kG seed magnetic field.

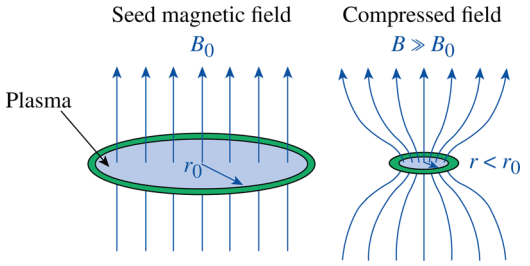

FIG. 1. In the concept of magnetic-flux compression, a seed magnetic field is embedded into a conductor (plasma). The conductor traps the field, such that upon compression of the material, the field is compressed as well.

To efficiently compress magnetic flux embedded over a region of characteristic size R, the compression time τ_c must be shorter than the diffusion time τ_m. This condition is equivalent to requiring a large magnetic Reynolds number $R_m \equiv \tau_m/\tau_c > 1$. The compression time can be written as $\tau_c = R/V_i$, with V_i being the implosion velocity. The diffusion time can be expressed as $\tau_m = R^2/D_m$, in which D_m is the magnetic diffusivity. Using the classical theory of collisional plasmas,[13] the magnetic diffusivity of hydrogen plasma in units of cm^2/s is $D_m \approx 8.2\times10^5\, T_e^{-3/2}\,\ln\Lambda$, where T_e is the electron temperature in eV and ln Λ is the Coulomb logarithm. Consequently, the condition $\tau_c < \tau_m$ yields a lower limit for the implosion velocity in cm/s of

$$V_i > \frac{D_m}{R} \approx 8.2\times10^9 T_e^{-1.5}\frac{\ln\Lambda}{R}, \qquad (1)$$

where R is in μm.

Applying this equation to the conditions in an ICF capsule shows that an embedded field is predominantly trapped in the ionized gas fill inside the shell. A laser pulse incident onto an ICF target filled with D_2 or DT gas launches a spherically converging shock through the shell. Upon breakout into the gas at the inner shell boundary, the gas fill is heated to temperatures of the order of ~100 eV and becomes fully ionized. As the relatively cold shell implodes, the gas temperature increases further, reaching several keV at peak compression. The hot ionized gas quickly becomes a good enough conductor capable of trapping the magnetic field. Employing Eq. (1) and using $T_e = 100$ eV, $R = 100$ μm, and ln $\Lambda = 7$, the implosion velocity required for efficient flux compression within the gas fill is $V_i > 6\times10^5$ cm/s, more than an order of magnitude below the characteristic implosion velocity for an ignition target. The *shell* of an ignition target is not a good enough conductor to trap the field.

Substituting typical values for the shell ($T_e = 10\,\text{eV}$, $R = 30\,\mu\text{m}$, and $\ln\Lambda = 5$), one finds $V_i > 4 \times 10^7$ cm/s, a value that exceeds typical implosion velocities in an ICF experiment.

Assuming a magnetic field B_0 with open field lines penetrating a plasma with a cross-sectional area of πR_0^2, and neglecting diffusion, the field compression can be expressed through conservation of the magnetic flux, i.e., $\Phi_0 = B_0\pi R_0^2 = \Phi_1 = B_1\pi R_1^2$, with $R_0 > R_1$. The compressed field scales with the reduction of the encircled area and can be written as

$$B_1 = B_0\left(\frac{R_0}{R_1}\right)^2. \tag{2}$$

Taking into account the diffusion of the magnetic field into the plasma shell as a result of its finite resistivity, Eq. (2) is modified to[28]

$$B_1 = B_0\left(\frac{R_0}{R_1}\right)^{2(1-1/R_m)}, \tag{3}$$

which highlights the requirement of a large magnetic Reynolds number. It is noteworthy that these equations apply to both the cylindrical and spherical scenarios discussed in this paper.

The target implosion hydrodynamics should not be directly affected by the presence of the magnetic field since the plasma beta, i.e., the ratio of hydrodynamic pressure to magnetic pressure is always much larger than one during the capsule evolution ($\beta \gg 1$). Similarly, an indirect influence of the magnetic field on the implosion history prior to peak compression, e.g., via changes in the laser absorption through modification of the electron conductivity, is negligible (see also the discussion of Fig. 10 and Sec. VI).

III. THE MIFEDS EXPERIMENTAL PLATFORM

To reach multimegagauss fields in a magnetic-flux–compression experiment, a sufficient seed magnetic field is necessary. Supplying this to the target chamber center of the OMEGA Laser Facility is nontrivial. The parametric space for implementing a seed-field generator is restricted on one side by the small physical volume available and the required unobstructed laser paths onto the implosion target and on the other side by the need for high energy in the magnetic pulse.

The experimental platform developed for this purpose is the MIFEDS device,[29] a drawing of which is shown in Fig. 2(a). The device fits into a standard diagnostics port on the OMEGA target chamber and comprises a vacuum enclosure containing a high-voltage charging power supply, capacitors, a laser-triggered spark-gap switch, and control circuits. It stores up to ~100 J of energy and is capable of delivering a multiple-tens-of-kA discharge current in an ~400-ns pulse. The current is directed through a transmission line that is connected to the vacuum housing via an interface flange. A coil is attached to the front of the transmission line, which typically is positioned at the center of the OMEGA target chamber. Using different coil shapes and sizes provides different magnetic field topologies and strengths. Examples of coils used in experiments are shown in Fig. 2(b). For the experiments described in this paper, Helmholtz-type coils and single coils were used, providing uncompressed magnetic-field strengths of ~50 and ~80 kG at the center of the coil assembly.

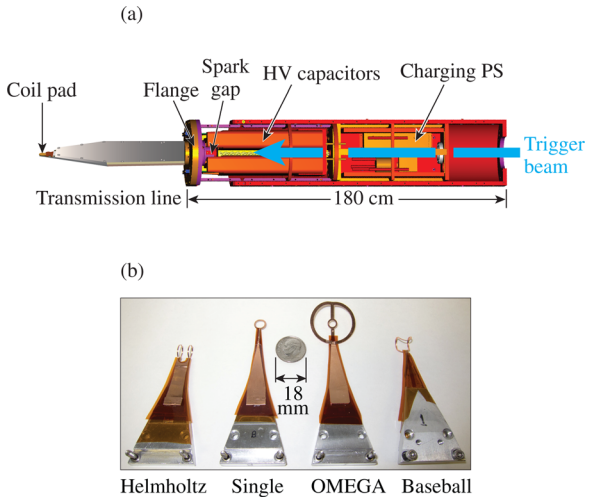

FIG. 2. (a) A schematic view of MIFEDS. The device's vacuum enclosure contains energy storage and trigger components to drive a strong current through a coil attached to the end of the transmission line, thereby generating magnetic fields of tens of kilogauss at the coil center. (b) Various types of coils used in experiments.

IV. MAGNETIC-FLUX COMPRESSION IN CYLINDRICAL TARGETS

An initial series of flux-compression experiments were carried out by embedding a seed magnetic field into cylindrical targets and are discussed in Refs. 28 and 30. The field was generated via the discharge of the MIFEDS device through a Helmholtz-type coil with the compression target placed on axis midway between the coils. Figure 3 shows a photograph of the experimental setup inside the OMEGA target chamber. The cylindrical target with a radius of 430 μm was imploded using 40 beams of the OMEGA Laser with a 1-ns square pulse at an averaged intensity of 5×10^{14} W/cm^2 and configured with SG4 distributed phaseplates (DPPs),[31] polarization

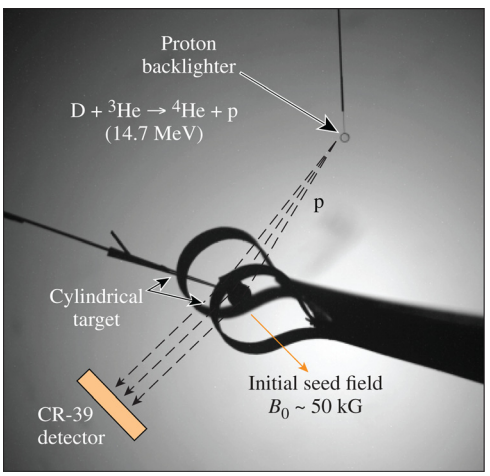

FIG. 3. Photograph of a cylindrical target surrounded by magnetic-field coils, generating an ~50 kG seed field. The field is probed using protons generated in the fusion reactions from a laser-heated D^{3}He target. The protons are deflected off their initial trajectories in the compressed magnetic field and are detected using a CR-39 track detector.

smoothing,[32] and full-bandwidth smoothing by spectral dispersion (SSD).[33]

The total neutron yield as well as the ion temperature were inferred from neutron time-of-flight (nTOF) diagnostics.[34] To measure the compressed field during the interaction, a proton backlighter based on the method described in Refs. 35–37 was used. The backlighter targets were positioned 9 mm from target chamber center opposite a CR-39 filter stack at a distance of 10.5 cm that measured the spatial proton distribution. The backlighters were 400-μm-diameter glass spheres filled with 10 atm of a D-^{3}He gas mixture. They were imploded by 20 OMEGA beams with 1-ns square pulses and focused to 300 μm. This heated the gas fill and caused the D and ^{3}He to undergo fusion reactions resulting in a monoenergetic ($\Delta E/E \sim 0.03$), point-like (size/object distance $\sim$0.01), and time-gated ($\sim$150 ps) proton burst[35] at $\sim$15 MeV.[38] An estimated proton backlighter yield of 3×10^8 gives a flux of 0.3 protons per μm^2 at the target.[36]

As illustrated in Fig. 4, the strongly compressed magnetic field in a magnetized ICF implosion is limited to the hot spot, while the dense shell contains a much smaller residual field. Protons from the backlighter are deflected into a characteristic two-peak pattern. The position of a proton on the detector relative to the point of detection, assuming an unperturbed trajectory, is related to the proton path integrated magnetic field via $\langle R_B B\rangle \approx \theta m_p v_p/e$, where R_B is the proton path under the action of the magnetic field B, θ is the deflection angle, m_p and v_p are the proton mass and velocity, and e is the proton charge. Protons traversing through the hot spot experience the strongest deflection and accumulate in the peak farthest from the center of the image (the top, red area on the detector in Fig. 4). These protons are slowed down slightly as they lose energy through collisions in the dense shell. A second, less deflected peak (blue) is caused by the protons that propagate through the lower-field shell but miss the high-field hot spot. These protons are slowed down more than the particles accumulated in the first peak, as they propagate through more dense material. This is a useful property since with a CR-39 detector the proton energy can be extracted from the track diameter that they leave when depositing their energy on the detector. This makes it possible to discriminate between the hot spot, strong-field traversing protons, and the background free-space particles that land in the same area of the detector.

A simulation package based on the Monte Carlo particle-transport framework GEANT4 (Ref. 39) was developed to predict and interpret the experimental data. After including field topology and material parameters predicted by the *LILAC*-MHD code (see Sec. VI) for the time of proton probing, GEANT4 computes the deflection pattern under the combined action of the field and scattering energy loss processes.

A comparison of experimental data (solid lines) with a 56-kG seed field and the numerical prediction (dotted lines) is shown in Fig. 5 for different proton energy bands.[30] The shaded areas in Fig. 5 highlight the position of the deflection peaks using the same color coding as in Fig. 4. The calculations are in good agreement with the experimental data and capture the observed double-peak deflection pattern well. The protons that were slowed down the most (labeled as <14.4 MeV) crossed through the shell but not the hot spot, missing the peak field. From the peak deflection of 1.9 ± 0.1 cm, one can estimate an average product $\langle R_B B\rangle \approx 0.1$ MG cm. Using a predicted hot-spot radius of $R_h = 0.5R_B = 17$ μm, this corresponds to an averaged hot-spot field of 30 ± 2 MG,[28,30] which exceeds the 10-MG threshold for magnetizing the electrons inside a hot spot (Sec. I). This maximum-field result represents a most conservative estimate, given by the lowest field B that can result in the observed deflection without violating the flux conservation condition $\Phi = B\pi R_h^2 \leq \Phi_0 \approx 0.3\,\text{kG}\,\text{cm}^2$. This can be calculated via $B = \pi\langle R_h B\rangle^2/\Phi$ and assuming no flux is lost, i.e., $\Phi = \Phi_0$. The extracted field compression of $\sim$530 is consistent with Eq. (2) and a convergence ratio of $\sim$24. If a more realistic case is considered, where initial flux is lost through diffusion, i.e., $\Phi < \Phi_0$, the magnetic field must be revised upward to match the observed deflections.

For the cylindrical experiments, the amplified magnetic field's effect on the neutron yield was expected to be negligible. The hot ions most likely to undergo fusion reactions (at the Gamow peak) are in the kinetic regime with their mean free path being comparable to the hot-spot radius. For hot-spot conditions where $n_e = 8 \times 10^{22}\,\text{cm}^3$ and $T_h = 1.5$ keV, the Gamow peak is at 8.2 keV. These ions will undergo only few collisions before leaving the hot spot. The electrons are fully magnetized but are thermally decoupled from the ions

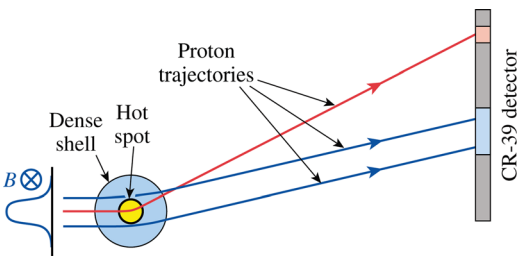

FIG. 4. Protons propagating through an imploded target are deflected by the compressed magnetic field and are detected using a CR-39 track detector. The compressed magnetic field peaks in the center of the hot spot and has a tail that extends into the shell, resulting in a two-peak deflection pattern.

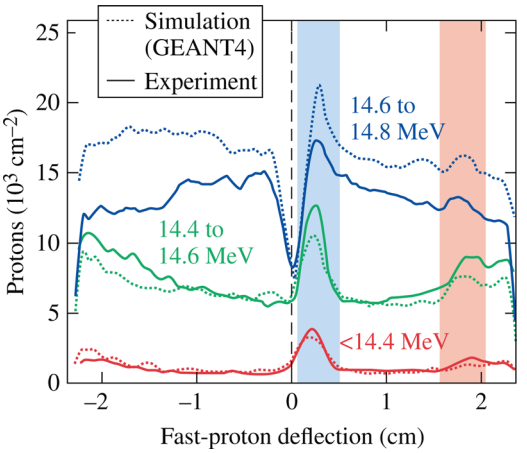

FIG. 5. Comparison of experimental and computational results of the proton deflection pattern from a cylindrically compressed target with a 56-kG seed field.

since the thermal equilibration time is of the order of 100 ps. As such, no fusion performance enhancement was observed for magnetized cylindrical implosions.

V. MAGNETIC-FLUX COMPRESSION IN SPHERICAL TARGETS

MIFEDS was employed in a setup similar to the cylindrical target experiments to embed magnetic fields into spherical targets.[11] Spherical CH targets with a radius of 430 μm and a wall thickness between 23.1 and 24.5 μm were imploded using 40 beams of the OMEGA Laser delivering an averaged intensity of $\sim 7 \times 10^{14}$ W/cm^2. The laser was configured with a 1-ns square pulse, SG4 DPPs, polarization smoothing, and full-bandwidth SSD. The capsules were filled with room-temperature D_2 gas at pressures of 3–10 atm.

To verify the field compression in spherical geometry, proton deflectometry was employed in conjunction with a Helmholtz-type coil generating a seed field of 50 kG. While the straight field lines from a Helmholtz-coil setup will remain straight upon cylindrical compression, this is not the case for spherical targets, as is illustrated in Fig. 6. The field topology in a spherically compressed target is inherently more complicated than the cylindrical case. For cylindrical targets, the low signal-to-noise of the proton backlighter signal could be alleviated by integrating the proton signal along the direction of the cylinder axis. For spherical targets, this is not possible, and only very few protons will be deflected from their original propagation path by traversing through the intrinsically smaller high-field region inside the target.

A calculation for such a deflection is shown in Fig. 7 as the red line. The target was assumed to consist of a 20-μm-radius hot spot containing a homogeneous 26-MG magnetic field, surrounded by a 5-μm shell. This was probed assuming a 15.2-MeV, monoenergetic proton point source, 9 mm away from the target. The proton trajectories and impact position onto a detector 10.5 cm away from the target were calculated using the momentum equation including the Lorentz force as well as a friction term describing the slowing of fast ions via collisions with plasma electrons. Slowing through ion-ion collisions is roughly a factor of 1000 lower and was neglected, as was ion-ion scattering. Despite the more complicated topology of a spherically compressed magnetic field compared to the cylindrical compression, the proton deflection pattern in Fig. 7 still exhibits the two-peak characteristic introduced in Sec. IV. As in the cylindrical case, these data exhibit two pronounced peaks, the farthest one at ~1.5 cm

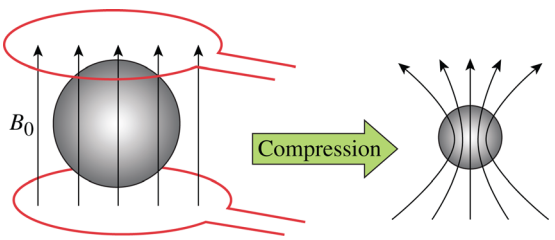

FIG. 6. The compression of a spherical target with initially straight magnetic seed field lines adds a strong radial component to the magnetic-field topology.

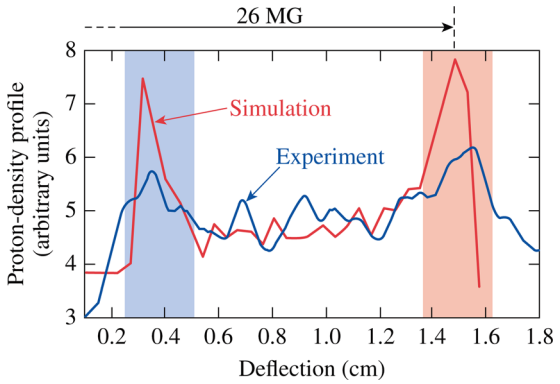

FIG. 7. Simulated (red) and experimental (blue) proton deflectometry data from a magnetized spherical implosion. The simulation assumed a 26-MG uniformly magnetized hot spot with a 20-μm radius. The experimental data are from a spherical implosion of a 50-kG seed field.

being caused by protons propagating through the high-field hot spot.

The blue line in Fig. 7 shows the experimental proton density data from a spherical implosion, as measured by the CR-39 track detector. These data were obtained using a 50-kG seed field in a target with a 5-atm D_2 gas fill. In these data two peaks are discernible, the location of which are consistent with the simulated lineout, suggesting a ~26-MG magnetic field inside the hot spot of the spherical target. The flux-limited minimum field that agrees with the measured $\langle R_h B \rangle = 0.04$ MG cm calculates to $B_{min} = 20$ MG, and a 26 MG field implies a convergence ratio of ~27 and a magnetic-flux loss of roughly 30%. While the data in Fig. 7 constitute the only measurement of the magnetic field inside a spherically compressed target, the extracted field amplification agrees well with the results from cylindrical implosions. This is shown in Fig. 8, which plots compressed field results of the laser-driven flux-compression experiments as a function of the seed-field strength. The green diamonds are from the cylindrical experiments discussed in Sec. IV, and the red circle corresponds to the spherical implosion data presented in Fig. 7. A linear fit through the cylindrical data yields an amplification factor of ~550.

To achieve an optimum fuel assembly performance in an ICF experiment, it is important that the capsule implodes

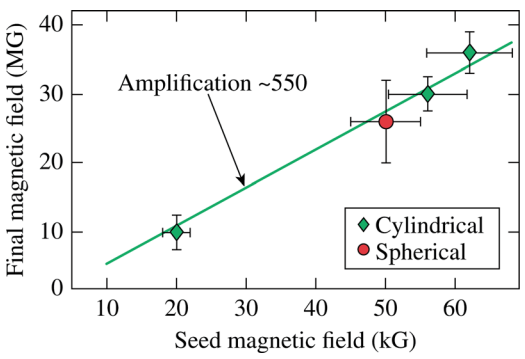

FIG. 8. Experimentally measured final magnetic field in laser-driven flux-compression experiments as a function of the seed-field strength. Green diamonds are from cylindrical implosions discussed in Sec. IV; the red circle corresponds to the spherical implosion data in Fig. 7. The experiments yield a field amplification factor of ~550.

uniformly. Compared to a full 60-beam implosion experiment on OMEGA, the presence of the seed coils in the magnetized ICF setup compromises the irradiation uniformity since it blocks laser beams from illuminating the target. To ensure optimized implosion uniformity in spherical geometry with a reduced number of drive beams, a single-coil assembly was used to generate the magnetic fields. This was combined with a 40-beam laser setup for polar-drive applications.[40] Using a single coil provides magnetic seed fields of larger magnitude—in this case ~80 kG at the center of the coil. The single-coil experimental setup is shown in Fig. 9.

In the single-coil setup an x-ray backlighter diagnostic was used to assess the implosion uniformity.[41] The backlighter target was a 25-μm-thick Au foil mounted 5 mm away from the target at 52.6° off the equatorial plane (Fig. 9). The foil was illuminated using four OMEGA Laser beams with a total of 1.8 kJ and focused to ~700 μm, generating x rays in the range of 2.5–4.5 keV. After passing through an imploding target, the x rays were imaged onto a fast x-ray framing camera,[42] generating radiography data at multiple times during the target implosion. The ICF target performance was measured via nTOF diagnostics.[34]

X-ray–backlit images of imploded spherical targets with and without an applied seed field are displayed in Fig. 10. The images are plotted using the same spatial scale and color map. The MIFEDS coil was present around the target in both cases and the images were taken at ~2 ns, a few hundred ps before peak compression. The bright area is the heated gas at the center of the target; the dark region surrounding it results from x rays being absorbed in the dense shell and the coronal plasma. The center appears slightly brighter than the background since at this time, the self-emission from the compressed core starts to exceed the backlighter emission. The implosion is very uniform despite using only 40 beams. No discernible difference can be observed between the field and no-field cases, confirming that the magnetic field has no impact on the implosion uniformity.

In Ref. 43 it is documented that the shell thickness is an important parameter in an ICF implosion, with the performance decreasing for thicker shells at a given laser-drive

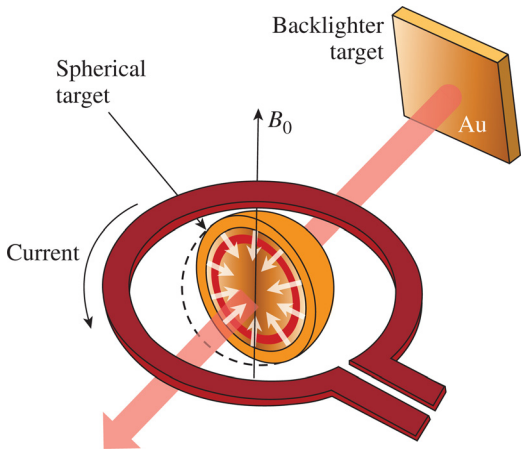

FIG. 9. A spherical target is placed at the center of a single coil seeding a magnetic field of 80 kG. The implosion uniformity is tracked by radiographing the target using x rays from a laser-irradiated Au foil.

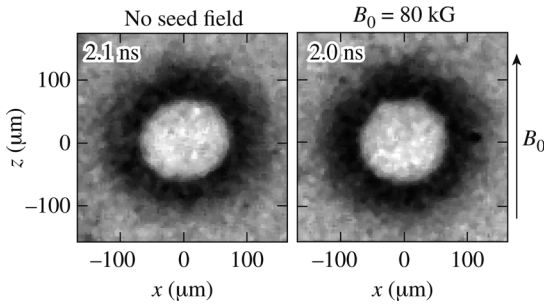

FIG. 10. X-ray–backlit images of a spherical implosion at ~400 ps before peak compression show no discernibly difference between nonmagnetized implosions (left) and implosions with a seed magnetic field (right).

configuration. This can be understood by considering both the ion temperature and consequently the neutron yield scale with the implosion velocity[8] (Sec. I). Because of energy balance, the implosion velocity decreases if more mass needs to be accelerated, such that an increase in shell thickness by a few μm will have a considerable effect on the fuel assembly performance.

Figure 11 shows the measured neutron yield and the ion temperature from shots with an applied seed field of 80 kG (red circles) and without magnetic fields (blue squares). These data were taken with a 10-atm D_2 gas fill and are plotted as a function of the target-shell thickness. To separate the effect of the magnetic field and the shell thickness on the neutron yield Y_n and the ion temperature T_i, a multiple linear regression method is used. To that end, these quantities are expressed as $Y_n = Y_{n0} + A_B B_0 + A_\Delta \Delta$ and $T_i = T_{i0} + C_B B_0 + C_\Delta \Delta$, with

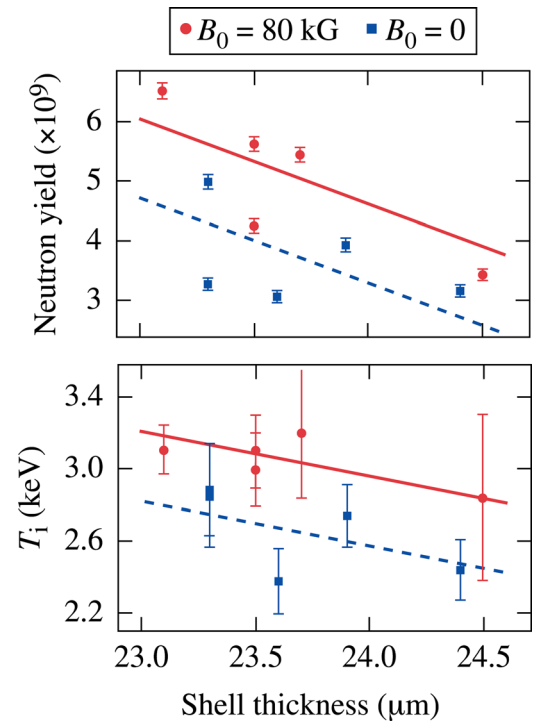

FIG. 11. Experimental neutron yield and ion temperature plotted against shell thickness. Performance for magnetized implosions (red dots) is enhanced compared to the nonmagnetized ones (blue squares). Fits to the data reveal an ion-temperature enhancement of 15% and a neutron-yield increase of 30% in the presence of the magnetic field (solid lines) compared to nonmagnetized implosions (dashed).

TABLE I. Multiple linear regression coefficients for the fits to the experimental data in Fig. 11.

	Y_{n0}	A_B (10^{-5}/G)	A_Δ (1/μm)
	T_{i0}	C_B (10^{-6}/G)	C_Δ (1/μm)
Y_n ($\times 10^9$)	37.6	1.7 ± 0.6	-1.4 ± 0.6
T_i (keV)	8.57	4.8 ± 1.3	-0.25 ± 0.11

B_0 being the seed field (0 or 80 kG) and Δ being the shell thickness. A least square fit to the data yields the fitting parameters as listed in Table I. The goodness of the fit is assessed through an F test giving a large F ratio of 6.0 for the neutron yield and 7.3 for the ion temperature. This corresponds to a better-than-95% degree of confidence. The result of the linear regression method is plotted as the solid lines in Fig. 11 (red for the magnetized targets, dashed blue for the nonmagnetized implosions). This shows a clear enhancement of both the neutron yield and the ion temperature. For shots where the magnetic field was applied, the yield was enhanced by ~30% and the ion temperature by ~15%. The data shown in Fig. 11 represent the first measurement of a fusion performance enhancement resulting from embedding a strong magnetic field into an ICF capsule, thereby magnetizing the hot spot.[11]

VI. NUMERICAL SIMULATION

The 1-D hydrodynamics code *LILAC* (Ref. 44) is the primary tool used at LLE for target design and simulations of ICF implosions. This code has been modified to solve the resistive MHD equations including Braginskii's corrections to the thermal conductivity (*LILAC*-MHD).[45] This modified version was used to simulate the laser-driven magnetic-flux–compression experiments.

For cylindrical implosions (Sec. IV), the initially straight field lines remain largely straight during compression and the magnetized cylindrical target can be treated in 1-D (see discussion in Refs. 28 and 30). Applying a 1-D simulation to the inherently three-dimensional problem of the magnetic field in a spherically compressed target is necessarily limited because of the field line distortion and the generation of a radial field component during the compression (Fig. 6).

To understand the compressed field topology in spherical targets, a 2-D, azimuthally symmetric B-field model was incorporated into *LILAC*. The new code (*LILAC*-MHD-Sp) solves the 1-D hydrodynamic equations including effective magnetic-field pressure and thermal conductivity with polar-angle–averaged Braginskii's corrections. The 2-D field structure, i.e., the radial and polar (theta) components of the magnetic field, is calculated by solving the 2-D induction equation for the azimuthal component of the vector potential. This dimensional split is motivated by the fact that the magnetic-field pressure and tension are much smaller than the plasma pressure ($\beta \gg 1$). The target dynamics is approximately one dimensional and independent of the magnetic field. The magnetic-field lines are compressed in the gas perpendicularly to the direction of the field, causing pinching of the magnetic-flux tube around the shell equator. Figure 12 shows the magnetic field at peak compression computed by

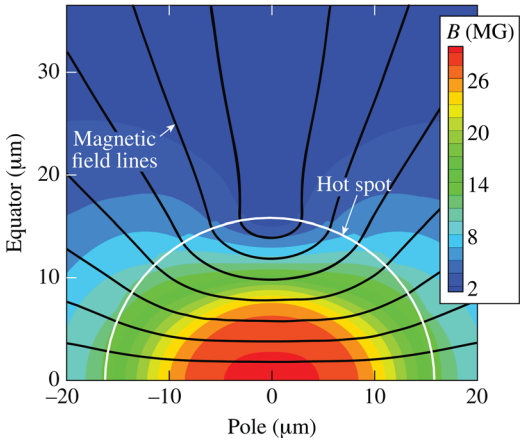

FIG. 12. Result from a 2-D post-processed 1-D simulation of a magnetized spherically imploding target. The black lines represent magnetic-field lines, and the color denotes field strength. In this simulation, the initial seed field of 50 kG has been compressed to ~25 MG inside the hot spot.

LILAC-MHD-Sp for a magnetized spherical implosion experiment on OMEGA with a 50-kG seed field. The field lines are shown in black, the color contours represent the magnitude of the field, and the outline of the hot spot is shown in white. The simulation gives a line-averaged compressed field of about 25 MG.

The heat-flux in the presence of a strong magnetic field is suppressed only perpendicular to the field lines, with the electrons streaming freely parallel to the field direction. From Fig. 12 it is clear that a large fraction of a spherical target's surface is subject to open field lines such that the uninhibited losses in that direction must be taken into account to correctly simulate the spherical problem. To implement this into *LILAC*-MHD, the overall electron thermal conductivity κ_{tot} was described as a superposition of both the parallel and perpendicular contributions, $\kappa_\parallel$ and $\kappa_\perp$, via the equation $\kappa_{tot} = \kappa_\parallel A_\parallel / A_{tot} + \kappa_\perp A_\perp / A_{tot}$. $A_\parallel$ and $A_\perp$ are the parallel and perpendicular projections of the total hot-spot area A_{tot}, respectively. This treatment reveals an important limitation of the experiments discussed in the preceding sections. Since the current setup generates open magnetic-field lines inside the compression target, there is a limit to the achievable heat-loss suppression imposed by the target geometry. In a perfectly spherical scenario, even if all perpendicular heat losses are suppressed, the remaining parallel-field losses are still 50% of the total losses without a magnetic field. Ultimately, this limitation can only be overcome by introducing a closed-field-line topology to the target (see Sec. VII).

The simulations show no indication of the magnetic field affecting the implosion history of the capsule (as opposed to the fusion performance around peak compression), e.g., through a change of the heat transport in the ablation layer. This was tested by artificially turning off any magnetic field effects in the simulations until after the laser had turned off. A change in fusion performance can therefore be attributed solely to the magnetization of the hot spot. Figure 13 shows simulation results for a spherical implosion using the target parameters of the spherical experiments discussed in Sec. V (24-μm shell thickness, filled with D_2 at 10 atm). The lines in Fig. 13 show ion temperature profiles at peak neutron yield,

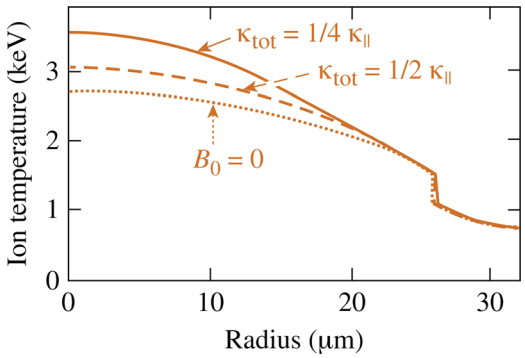

FIG. 13. Ion-temperature profiles at the center of a spherical target, as simulated by *LILAC*-MHD at the time of peak neutron yield for an initial seed-field value of 0 (dotted line) and 80 kG. The dashed line is calculations assuming a reduction of the heat conduction by 1/2; the solid line assumes a reduction to 1/4 of the unmodified value.

without an applied magnetic field (dotted line) and using an 80-kG seed field (dashed and solid lines). As expected, in the presence of a magnetic seed field, the ion temperature increases across the hot spot. Assuming full suppression of the perpendicular heat losses ($\kappa_{tot} = 1/2\kappa_{\|}$), the calculated increase in ion temperature at the target center through magnetization of the hot spot is 8% (dashed line), corresponding to a volume-integrated neutron-yield enhancement of 13%. This is in contrast to the experimental results for spherical targets (see Sec. V), where an ion-temperature enhancement of 15% and a neutron-yield increase of 30% were measured. The experimental result can be recovered in the 1-D simulations by assuming a reduction of the total heat conduction to one quarter of the unperturbed value, i.e., $\kappa_{tot} = 1/4\kappa_{\|}$. Simulation results using this artificial reduction are plotted in Fig. 13 as the solid line. Using the geometry argument from above for implementing the heat conduction in the simulations, this ratio would imply a prolate distortion of the hot spot such that the area perpendicular to the magnetic-field lines is $A_{\perp} \approx 3A_{\|}$. This interpretation is not supported, however, by the x-ray radiography data (Fig. 10), which show a uniform hot spot at least up to a few hundred ps before peak compression. The 1-D simulations are too simplified to fully capture the inherently 2-D heat transport in a spherically compressed target. If the parallel heat losses are fully inhibited and $\kappa_{tot} = 0$ [i.e., via closing the field lines (see Sec. VII)], the simulations predict an increase of 42% in the ion temperature and a 73% neutron- yield enhancement. In this case, the target performance is primarily limited by radiative energy losses.

VII. CLOSED MAGNETIC-FIELD LINES

There are various paths to generating a closed-field-line topology inside an ICF target; two potential methods are shown in Fig. 14. Driving a current through the center of a capsule using a thin wire [as illustrated in Fig. 14(a)] would create an azimuthal seed field with closed field lines. Upon launching the compression drive, the driven shock wave ionizes the gas fill such that it becomes conductive and traps the magnetic field. After the external current is terminated, internal currents are induced in the plasma (shown in red), keeping the magnetic field "frozen in." The magnetization of a hot spot with these magnetic-field characteristics will therefore cause heat-flux suppression in 4π.

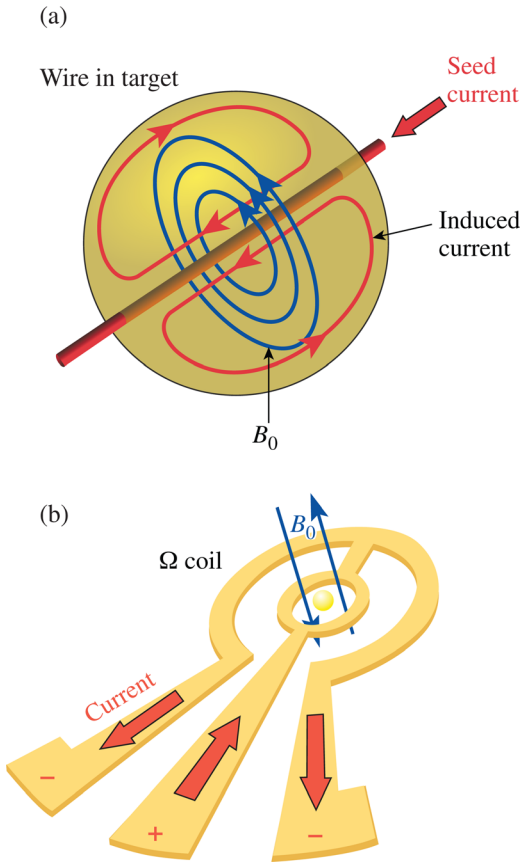

FIG. 14. Potential setups to generate closed field lines inside an ICF target. (a) A wire through the target generates an azimuthal magnetic field (blue) that is trapped inside by inductively driven currents (red). (b) The current in the same direction on either side of the inner loop of an Ω-coil generates a bi-directional field at the coil's center. Upon target compression, this can cause reconnection of the field lines and therefore a closed-field topology.

Alternatively, plasma currents similar to those shown in Fig. 14(a) can be induced by forcing reconnection of a bi-directional magnetic field. This can be generated by a coil as shown in Fig. 14(b) [see also Fig. 2(b)], where the field-generating current propagates in the same direction on either side of the inner loop. The target compression in the center of the loop will then generate currents similar to the case in Fig. 14(a) (red), keeping the magnetic field trapped. Assuming a "frozen" field, the initial open-field line topology will be maintained. If the volume containing the field is compressed sufficiently, however, it is possible that the topology will change and the magnetic-field lines can become closed from the effect of magnetic reconnection.[46]

VIII. CONCLUSION

Strong magnetic fields of tens of kilogauss were embedded into both cylindrical and spherical implosion targets. These were driven by 40 beams of the OMEGA Laser, resulting in high implosion velocities that trap the magnetic field inside the capsule, thereby compressing it by several orders of magnitude. These magnetic fields were measured

using the deflection of protons emitted from a glass microballoon filled with D^3He gas in both cylindrical and spherical geometry, giving averaged fields inside the hot spot of several tens of megagauss, sufficient to magnetize the hot spot. The implosion of magnetized and nonmagnetized spherical targets was confirmed to be uniform by using x-ray radiography. At the magnetic fields reached in these magnetic-flux–compression experiments, the hot spot inside a spherical target becomes strongly magnetized, suppressing the perpendicular heat flow by confining the electrons. This increases the temperature inside the hot spot and, consequently, the neutron yield. The measurements represent the first experimental verification of this effect with an observed ion-temperature enhancement of ~15% and a neutron-yield increase of ~30% compared to the unmagnetized case.

This work has been supported by the U.S. Department of Energy under Cooperative Agreement Nos. DE-FC02-04ER54789 and DE-FC03-92SF19460.

[1]J. Nuckolls, L. Wood, A. Thiessen, and G. Zimmerman, Nature **239**, 139 (1972).
[2]J. D. Lindl, *Inertial Confinement Fusion: The Quest for Ignition and Energy Gain Using Indirect Drive* (Springer-Verlag, New York, 1998).
[3]S. Atzeni and J. Meyer-ter Vehn, *The Physics of Inertial Fusion: Beam Plasma Interaction, Hydrodynamics, Hot Dense Matter, International Series of Monographs on Physics* (Clarendon Press, Oxford, 2004).
[4]S. E. Bodner, D. G. Colombant, J. H. Gardner, R. H. Lehmberg, S. P. Obenschain, L. Phillips, A. J. Schmitt, J. D. Sethian, R. L. McCrory, W. Seka, C. P. Verdon, J. P. Knauer, B. B. Afeyan, and H. T. Powell, Phys. Plasmas **5**, 1901 (1998).
[5]R. L. McCrory, D. D. Meyerhofer, S. J. Loucks, S. Skupsky, R. Betti, T. R. Boehly, T. J. B. Collins, R. S. Craxton, J. A. Delettrez, D. H. Edgell, R. Epstein, K. A. Fletcher, C. Freeman, J. A. Frenje, V. Y. Glebov, V. N. Goncharov, D. R. Harding, I. V. Igumenshchev, R. L. Keck, J. D. Kilkenny, J. P. Knauer, C. K. Li, J. Marciante, J. A. Marozas, F. J. Marshall, A. V. Maximov, P. W. McKenty, S. F. B. Morse, J. Myatt, S. Padalino, R. D. Petrasso, P. B. Radha, S. P. Regan, T. C. Sangster, F. H. Séguin, W. Seka, V. A. Smalyuk, J. M. Soures, C. Stoeckl, B. Yaakobi, and J. D. Zuegel, J. Phys. IV France **133**, 59 (2006).
[6]B. A. Hammel and National Ignition Campaign Team, Plasma Phys. Controlled Fusion **48**, B497 (2006).
[7]R. Betti, P. Y. Chang, B. K. Spears, K. S. Anderson, J. Edwards, M. Fatenejad, J. D. Lindl, R. L. McCrory, R. Nora, and D. Shvarts, Phys. Plasmas **17**, 058102 (2010).
[8]C. D. Zhou and R. Betti, Phys. Plasmas **15**, 102707 (2008).
[9]R. Betti and C. Zhou, Phys. Plasmas **12**, 110702 (2005).
[10]O. V. Gotchev, N. Jang, J. Knauer, M. Barbero, R. Betti, C. Li, and R. Petrasso, J. Fusion Energy **27**, 25 (2008).
[11]P. Y. Chang, G. Fiksel, M. Hohenberger, J. P. Knauer, R. Betti, F. J. Marshall, D. D. Meyerhofer, F. H. Séguin, and R. D. Petrasso, Phys. Rev. Lett. **107**, 035006 (2011).
[12]T. R. Boehly, D. L. Brown, R. S. Craxton, R. L. Keck, J. P. Knauer, J. H. Kelly, T. J. Kessler, S. A. Kumpan, S. J. Loucks, S. A. Letzring, F. J. Marshall, R. L. McCrory, S. F. B. Morse, W. Seka, J. M. Soures, and C. P. Verdon, Opt. Commun. **133**, 495 (1997).
[13]S. I. Braginskii, *Reviews of Plasma Physics*, edited by M. A. Leontovich (Consultants Bureau, New York, 1965).
[14]M. M. Widner, C. J. Chang, A. V. Farnsworth, Jr., R. J. Leeper, T. S. Prevender, L. Baker, and J. N. Olsen, Bull. Am. Phys. Soc. **22**, 1139 (1977).
[15]I. R. Lindemuth and R. C. Kirkpatrick, Nucl. Fusion **23**, 263 (1983).
[16]A. Hasegawa, H. Daido, M. Fujita, K. Mima, M. Murakami, S. Nakai, K. Nishihara, K. Terai, and C. Yamanaka, Phys. Rev. Lett. **56**, 139 (1986).
[17]W. H. Choe, Laser Part. Beams **8**, 477 (1990).
[18]R. C. Kirkpatrick, I. R. Lindemuth, and M. S. Ward, Fusion Technol. **27**, 201 (1995).
[19]T. Intrator, S. Y. Zhang, J. H. Degnan, I. Furno, C. Grabowski, S. C. Hsu, E. L. Ruden, P. G. Sanchez, J. M. Taccetti, M. Tuszewski, W. J. Waganaar, and G. A. Wurden, Phys. Plasmas **11**, 2580 (2004).
[20]S. A. Slutz, M. C. Herrmann, R. A. Vesey, A. B. Sefkow, D. B. Sinars, D. C. Rovang, K. J. Peterson, and M. E. Cuneo, Phys. Plasmas **17**, 056303 (2010).
[21]F. S. Felber, M. A. Liberman, and A. L. Velikovich, Appl. Phys. Lett. **46**, 1042 (1985).
[22]F. S. Felber, M. M. Malley, F. J. Wessel, M. K. Matzen, M. A. Palmer, R. B. Spielman, M. A. Liberman, and A. L. Velikovich, Phys. Fluids **31**, 2053 (1988).
[23]F. S. Felber, M. A. Liberman, and A. L. Velikovich, Phys. Fluids **31**, 3675 (1988).
[24]R. K. Appartaim and A. E. Dangor, J. Appl. Phys. **84**, 4170 (1998).
[25]J. H. Degnan, F. M. Lehr, J. D. Beason, G. P. Baca, D. E. Bell, A. L. Chesley, S. K. Coffey, D. Dietz, D. B. Dunlap, S. E. Englert, T. J. Englert, D. G. Gale, J. D. Graham, J. J. Havranek, C. D. Holmberg, T. W. Hussey, R. A. Lewis, C. A. Outten, R. E. Peterkin, D. W. Price, N. F. Roderick, E. L. Ruden, U. Shumlak, G. A. Smith, and P. J. Turchi, Phys. Rev. Lett. **74**, 98 (1995).
[26]J. H. Degnan, M. L. Alme, B. S. Austin, J. D. Beason, S. K. Coffey, D. G. Gale, J. D. Graham, J. J. Havranek, T. W. Hussey, G. F. Kiuttu, B. B. Kreh, F. M. Lehr, R. A. Lewis, D. E. Lileikis, D. Morgan, C. A. Outten, R. E. Peterkin, D. Platts, N. F. Roderick, E. L. Ruden, U. Shumlak, G. A. Smith, W. Sommars, and P. J. Turchi, Phys. Rev. Lett. **82**, 2681 (1999).
[27]A. D. Sakharov, Sov. Phys. Usp. **9**, 294 (1966).
[28]J. P. Knauer, O. V. Gotchev, P. Y. Chang, D. D. Meyerhofer, O. Polomarov, R. Betti, J. A. Frenje, C. K. Li, M. J.-E. Manuel, R. D. Petrasso, J. R. Rygg, and F. H. Séguin, Phys. Plasmas **17**, 056318 (2010).
[29]O. V. Gotchev, J. P. Knauer, P. Y. Chang, N. W. Jang, M. J. Shoup, III, D. D. Meyerhofer, and R. Betti, Rev. Sci. Instrum. **80**, 043504 (2009).
[30]O. V. Gotchev, P. Y. Chang, J. P. Knauer, D. D. Meyerhofer, O. Polomarov, J. Frenje, C. K. Li, M. J.-E. Manuel, R. D. Petrasso, J. R. Rygg, F. H. Séguin, and R. Betti, Phys. Rev. Lett. **103**, 215004 (2009).
[31]Y. Lin, T. J. Kessler, and G. N. Lawrence, Opt. Lett. **20**, 764 (1995).
[32]T. R. Boehly, V. A. Smalyuk, D. D. Meyerhofer, J. P. Knauer, D. K. Bradley, R. S. Craxton, M. J. Guardalben, S. Skupsky, and T. J. Kessler, J. Appl. Phys. **85**, 3444 (1999).
[33]S. P. Regan, J. A. Marozas, R. S. Craxton, J. H. Kelly, W. R. Donaldson, P. A. Jaanimagi, D. Jacobs-Perkins, R. L. Keck, T. J. Kessler, D. D. Meyerhofer, T. C. Sangster, W. Seka, V. A. Smalyuk, S. Skupsky, and J. D. Zuegel, J. Opt. Soc. Am. B **22**, 998 (2005).
[34]V. Y. Glebov, C. Stoeckl, T. C. Sangster, S. Roberts, G. J. Schmid, R. A. Lerche, and M. J. Moran, Rev. Sci. Instrum. **75**, 3559 (2004).
[35]C. K. Li, F. H. Séguin, J. A. Frenje, J. R. Rygg, R. D. Petrasso, R. P. J. Town, P. A. Amendt, S. P. Hatchett, O. L. Landen, A. J. Mackinnon, P. K. Patel, V. A. Smalyuk, J. P. Knauer, T. C. Sangster, and C. Stoeckl, Rev. Sci. Instrum. **77**, 10E725 (2006).
[36]J. R. Rygg, F. H. Séguin, C. K. Li, J. A. Frenje, M. J.-E. Manuel, R. D. Petrasso, R. Betti, J. A. Delettrez, O. V. Gotchev, J. P. Knauer, D. D. Meyerhofer, F. J. Marshall, C. Stoeckl, and W. Theobald, Science **319**, 1223 (2008).
[37]C. K. Li, F. H. Sguin, J. R. Rygg, J. A. Frenje, M. Manuel, R. D. Petrasso, R. Betti, J. Delettrez, J. P. Knauer, F. Marshall, D. D. Meyerhofer, D. Shvarts, V. A. Smalyuk, C. Stoeckl, O. L. Landen, R. P. J. Town, C. A. Back, and J. D. Kilkenny, Phys. Rev. Lett. **100**, 225001 (2008).
[38]D. G. Hicks, C. K. Li, F. H. Séguin, A. K. Ram, J. A. Frenje, R. D. Petrasso, J. M. Soures, V. Y. Glebov, D. D. Meyerhofer, S. Roberts, C. Sorce, C. Stockl, T. C. Sangster, and T. W. Phillips, Phys. Plasmas **7**, 5106 (2000).
[39]S. Agostinelli, J. Allison, K. Amako, J. Apostolakis, H. Araujo, P. Arce, M. Asai, D. Axen, S. Banerjee, G. Barrand, F. Behner, L. Bellagamba, J. Boudreau, L. Broglia, A. Brunengo, H. Burkhardt, S. Chauvie, J. Chuma, R. Chytracek, G. Cooperman, G. Cosmo, P. Degtyarenko, A. Dell'Acqua, G. Depaola, D. Dietrich, R. Enami, A. Feliciello, C. Ferguson, H. Fesefeldt, G. Folger, F. Foppiano, A. Forti, S. Garelli, S. Giani, R. Giannitrapani, D. Gibin, J. Gmez Cadenas, I. Gonzlez, G. Gracia Abril, G. Greeniaus, W. Greiner, V. Grichine, A. Grossheim, S. Guatelli, P. Gumplinger, R. Hamatsu, K. Hashimoto, H. Hasui, A. Heikkinen, A. Howard, V. Ivanchenko, A. Johnson, F. Jones, J. Kallenbach, N. Kanaya, M. Kawabata, Y. Kawabata, M. Kawaguti, S. Kelner, P. Kent, A. Kimura, T. Kodama, R. Kokoulin, M. Kossov, H. Kurashige, E. Lamanna, T. Lampn, V. Lara, V. Lefebure, F. Lei, M. Liendl, W. Lockman, F. Longo, S. Magni, M. Maire, E. Medernach, K. Minamimoto, P. Mora de Freitas, Y. Morita, K. Murakami, M. Nagamatu, R. Nartallo, P. Nieminen, T.

Nishimura, K. Ohtsubo, M. Okamura, S. O'Neale, Y. Oohata, K. Paech, J. Perl, A. Pfeiffer, M. Pia, F. Ranjard, A. Rybin, S. Sadilov, E. Di Salvo, G. Santin, T. Sasaki, N. Savvas, Y. Sawada, S. Scherer, S. Sei, V. Sirotenko, D. Smith, N. Starkov, H. Stoecker, J. Sulkimo, M. Takahata, S. Tanaka, E. Tcherniaev, E. Safai Tehrani, M. Tropeano, P. Truscott, H. Uno, L. Urban, P. Urban, M. Verderi, A. Walkden, W. Wander, H. Weber, J. Wellisch, T. Wenaus, D. Williams, D. Wright, T. Yamada, H. Yoshida, and D. Zschiesche, Nucl. Instrum. Methods Phys. Res. A **506**, 250 (2003).

[40]F. J. Marshall, R. S. Craxton, M. J. Bonino, R. Epstein, V. Y. Glebov, D. Jacobs-Perkins, J. P. Knauer, J. A. Marozas, P. W. McKenty, S. G. Noyes, P. B. Radha, W. Seka, S. Skupsky, and V. A. Smalyuk, J. Phys. IV France **133**, 153 (2006).

[41]O. L. Landen, D. R. Farley, S. G. Glendinning, L. M. Logory, P. M. Bell, J. A. Koch, F. D. Lee, D. K. Bradley, D. H. Kalantar, C. A. Back, and R. E. Turner, Rev. Sci. Instrum. **72**, 627 (2001).

[42]D. K. Bradley, P. M. Bell, O. L. Landen, J. D. Kilkenny, and J. Oertel, Rev. Sci. Instrum. **66**, 716 (1995).

[43]F. J. Marshall, J. A. Delettrez, V. Y. Glebov, R. P. J. Town, B. Yaakobi, R. L. Kremens, and M. Cable, Phys. Plasmas **7**, 1006 (2000).

[44]J. Delettrez, R. Epstein, M. C. Richardson, P. A. Jaanimagi, and B. L. Henke, Phys. Rev. A **36**, 3926 (1987).

[45]N. W. Jang, R. Betti, O. V. Gotchev, and D. D. Meyerhofer, Bull. Am. Phys. Soc. **51**, 144 (2006).

[46]E. Priest and T. Forbes, *Magnetic Reconnection: MHD Theory and Applications* (Cambridge University Press, Cambridge, 2000).